NANO LETTERS

pubs.acs.org/NanoLett Letter

Emergent One-Dimensional Charge Order at Domain Walls of Competing Charge-Density-Wave Orders

Zhongyi Cao,[⊥] Hui Chen,[*,⊥] Wen-Han Dong,[⊥] Yanhao Shi,[⊥] Qi Qi, Haitao Yang, and Hong-Jun Gao

Cite This: *Nano Lett.* 2026, 26, 5882−5890 Read Online

ACCESS | Metrics & More | Article Recommendations | Supporting Information

ABSTRACT: Competing electronic phases can generate emergent states at their nanoscale interfaces that do not exist in the bulk. Direct real-space visualization of such interfacial states, however, remains exclusive. Here, we report an emergent one-dimensional (1D) charge order confined to atomically sharp domain walls between competing charge density wave (CDW) orders in the rare-earth ditelluride $GdTe_2$. Using low-temperature scanning tunneling microscopy and spectroscopy, we resolve three distinct symmetry-breaking CDWs occupying spatially separated surface nanodomains. Supported by density functional theory, two originate from intrinsic bulk instabilities, while the third arises from surface-induced Fermi surface reconstruction at the non-van der Waals termination. Strikingly, the boundary between bulk- and surface-derived CDWs hosts a short-range, quasi-1D charge modulation and an emergent energy gap, indicating confined electronic states produced by competing orders. These findings establish CDW domain walls as nanoscale electronic interfaces, offering a promising platform for nanoscale CDW-based devices and domain-wall-defined functional architectures.

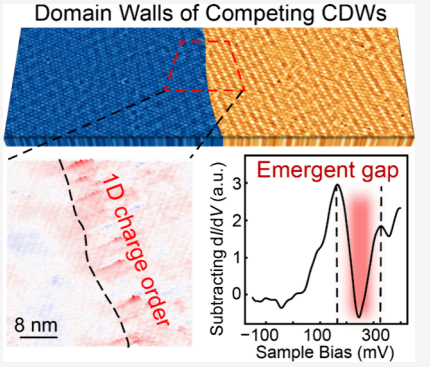

KEYWORDS: *domain wall, charge density wave, competing orders, rare-earth tellurides, scanning tunneling microscopy and spectroscopy*

Interfaces between competing symmetry-breaking electronic orders provide a fertile playground for emergent quantum phenomena. When distinct order parameters coexist, their mutual incompatibility can locally reconstruct electronic states, allowing new collective behavior to emerge at their boundaries. Domain walls (DWs) and boundaries of competing orders in quantum materials therefore act as nontrivial electronic interfaces rather than trivial defects, hosting low-dimensional states that are absent in the bulk.[1−6] Charge density waves (CDWs) represent one of the most fundamental classes of collective electronic states, characterized by periodic modulations of the electronic charge density accompanied by broken translational and point-group symmetries.[7,8] Owing to their sensitivity to commensurability, dimensionality, and components, CDW systems often host multiple competing or intertwined phases. Such competition has been widely studied through the interplay between CDWs and other ordered phases, including magnetism,[9,10] superconductivity,[11,12] and pair density waves.[13,14] A conceptually distinct route to emergent behavior arises from DWs between distinct CDW orders themselves, which provide a fertile platform for electronic states that are absent in the bulk and are therefore crucial for understanding and engineering novel quantum phenomena.[15−18]

Existing experimental studies of DWs in CDW systems have predominantly focused on boundaries between nanodomains of the same CDW order, differing only by phase, translational displacement, or closely related symmetry variants. For example, the DWs between commensurate and incommensurate CDW phases in 1T-phase transition metal dichalcogenides are proposed to nucleate superconductivity.[19−23] The symmetry-breaking CDWs such as unidirectional CDWs[24] and chiral CDWs[25,26] further introduce additional degeneracy in DW configurations. In contrast, DWs between distinct CDW orders with different symmetries or microscopic origins represent a qualitatively different class of interface, where incompatibility between order parameters can frustrate long-range order and potentially stabilize new electronic states. Layered rare-earth tellurides, RTe_n (R = rare-earth element; n = 2, 2.5, 3, 4), provide a promising platform for exploring such physics.[27−31] These materials host multiple CDW instabilities with comparable energy scales and exhibit strong sensitivity to lattice symmetry, reduced dimensionality, and surface termination. In particular, non-van der Waals (non-vdW) cleavage surfaces can substantially reconstruct the electronic structure, opening the possibility of surface-specific CDW orders that compete with bulk-derived instabilities. This combination naturally paves the way for DWs between CDWs of distinct symmetry and microscopic origin. However, direct real-space

Received: February 13, 2026
Revised: April 14, 2026
Accepted: April 15, 2026
Published: April 20, 2026

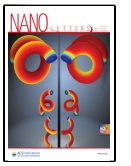

https://doi.org/10.1021/acs.nanolett.6c00774
Nano Lett. 2026, 26, 5882−5890

observation of emergent charge order at these interorder-parameter DWs of CDWs remains elusive.

In this work, we report the coexistence and competition of multiple CDWs at the surfaces of a representative RTe_2 compound, $GdTe_2$, using low-temperature scanning tunneling microscopy/spectroscopy (STM/S). In addition to a unidirectional CDW (CDW-I) globally existing in the family of RTe_n, we observe a bulk-derived bidirectional order (CDW-II) and, a previously unreported, surface-induced bidirectional CDW (namely CDW-III). These two bidirectional states are superimposed on CDW-I, respectively, forming two distinct spatially separated nanodomains at the surface of $GdTe_2$. Both CDW-II and CDW-III are strongly bias-dependent, while the newly discovered symmetry-breaking CDW-III exhibits surface-sensitive phase fluctuations. Density functional theory (DFT) calculations further indicate that CDW-I and CDW-II originate from the intrinsic bulk electronic properties and are mainly induced by electron−phonon coupling, whereas CDW-III potentially arises from Fermi surface reconstruction induced by surface effects from non-vdW terminations. Beyond the characterization of these individual CDW states, the key finding of our study lies at their interface. Specifically, at the boundary between CDW-II and CDW-III nanodomains, we observe an emergent short-range charge order (SCO) which appears only within a specific energy window and is accompanied by an emergent local energy gap. Spatially resolved amplitude and phase analyses indicate that this SCO originates from the order parameter incompatibility between CDW-II and CDW-III, indicative of nontrivial electronic interfaces.

$GdTe_2$ crystallizes in a tetragonal lattice with space group $P4/nmm$ and adopts a layered structure composed of alternating square Te layers and double Gd−Te layers (Figure 1a). Upon cleavage, the crystal preferentially separates between a Te layer and its adjacent Gd−Te layer, which are strongly coupled to each other beyond vdW interactions, indicative of notable surface effects such as localized charge inhomogeneities. The cleaved surface exhibits two distinct domains, labeled Domain-A and Domain-B, each characterized by distinct charge modulation patterns, as highlighted by the contrasting colors in Figure 1b. Importantly, no step edge or height discontinuity is observed at the boundary between the two domains, and the atomic lattice remains continuous, indicating that they reside on the same cleaved surface rather than distinct surface terminations.

We first study the charge modulations in Domain-A surface regions by analyzing the Fourier transform (FT) of topographic image where the coexistence of two distinct CDWs is revealed (Figure 1c). The FT displays Bragg peaks $\mathbf{q}_{GdTe}$ (marked by white circles) and a series of CDW wave vectors (Figure 1c). For convenience, we define the reciprocal lattice vectors as $\mathbf{q}_a^{GdTe} = (q, 0)$ and $\mathbf{q}_c^{GdTe} = (0, q)$, where $q = 2\pi/a_0$ and a_0 is the lattice constant of $GdTe_2$, and express all CDW wave vectors in this basis. One CDW exhibits unidirectional charge modulations, hereafter referred to as CDW-I, while the other forms a bidirectional pattern, denoted as CDW-II. The CDW vectors can be categorized into two groups, highlighted by green and blue circles in Figure 1c. The four vectors along the Γ−X direction marked by green circles are assigned to the unidirectional CDW-I, with an incommensurate modulation wave vector of approximately $\mathbf{Q}_1^{I} = (0.302\ q, 0)$. Additional peaks arise at $\mathbf{q}_a^{GdTe} - 2\mathbf{Q}_1^{I} = (0.396\ q, 0)$, $2\mathbf{Q}_1^{I} = (0.604\ q, 0)$ and $\mathbf{q}_a^{GdTe} - \mathbf{Q}_1^{I} = (0.698\ q, 0)$, reflecting higher-order peaks

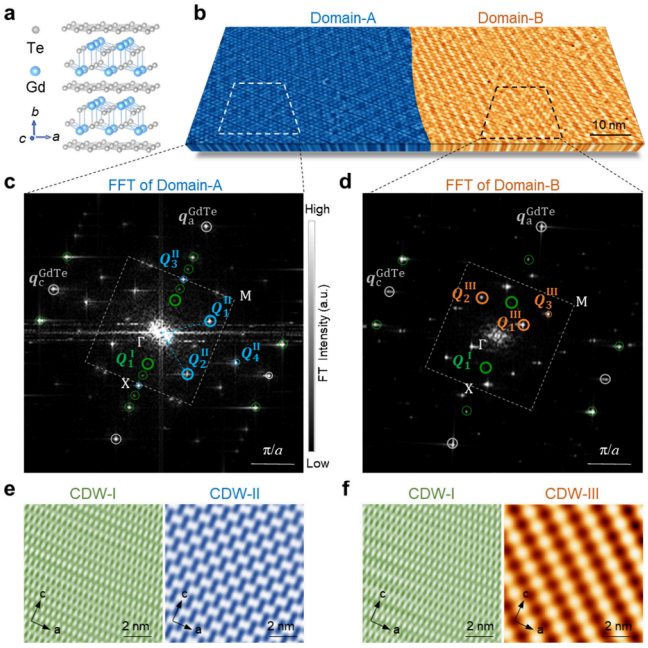

Figure 1. Observation of a domain boundary between two domains with distinct multiple CDW orders on the $GdTe_2$ surface. (a) Non-vdw layered structure of $GdTe_2$ crystal. (b) Three-dimensional STM topographic image of the as-cleaved $GdTe_2$ surface, showing two domains, A and B, highlighted by the blue and orange, respectively ($V_s = -1000$ mV, $I_t = 50$ pA). (c) FFT of the region of Domain-A in (b), showing two sets of CDWs: CDW-I (green circles) and CDW-II (blue circles). The Brillouin zone is marked by a white dashed square. (d) FFT of the region of Domain-B in (b), showing two sets of CDWs: CDW-I (green circles) and CDW-III (orange circles). (e) Filtered real-space images corresponding to the FFT in (c), showing the patterns of CDW-I (left) and CDW-II (right), respectively. (f) Filtered real-space images corresponding to FFT in (d), showing the pattern of CDW-I (left) and CDW-III (right), respectively.

from wave vector mixing.[32] To present the real-space pattern of CDW-I more clearly, the wave vectors related to CDW-I were filtered and zoomed in (left panel of Figure 1e). The spatially averaged dif ferential conductance (dI/dV) spectrum with a wide energy range exhibits a CDW energy gap of approximately 400 mV (Figure S1). CDW-I is observed across the entire sample surface, spanning both Domain-A and Domain-B. We therefore identify CDW-I as the globally established unidirectional CDW order in the RTe_n family, consistent with previous observations in MBE−grown $GdTe_2$ thin films.[33]

In addition to the $\mathbf{Q}_1^{III}$ of CDW-I, the remaining CDW vectors (blue circles in Figure 1c) are assigned to the bidirectional CDW-II, which is characterized by two primitive modulation vectors $\mathbf{Q}_1^{II} = (0.25\ q, 0.35\ q)$ and $\mathbf{Q}_2^{II} = (-0.25\ q, 0.35\ q)$. The additional peaks $\mathbf{Q}_3^{II}$ and $\mathbf{Q}_4^{II}$ can be represented as $\mathbf{Q}_3^{II} = \mathbf{Q}_1^{II} - \mathbf{Q}_2^{II} = (0.50\ q, 0)$ and $\mathbf{Q}_4^{II} = \mathbf{Q}_1^{II} + \mathbf{Q}_2^{II} = (0, 0.70\ q)$. Fourier-filtered real-space images show that CDW-II presents a quasi-hexagonal pattern in real space and preserves the same C_{2v} symmetry as CDW-I, despite its multidirectional modulation (Figure 1e). Additional STM measurements also confirm the independence of the two CDWs. First, the CDW patterns exhibit a strong bias dependence, as shown by topographic images taken at different bias voltages and their FFT cuts along the Γ−X direction (Figure S2). CDW-I persists across a wide bias range, whereas CDW-II only appears below

https://doi.org/10.1021/acs.nanolett.6c00774
Nano Lett. 2026, 26, 5882−5890

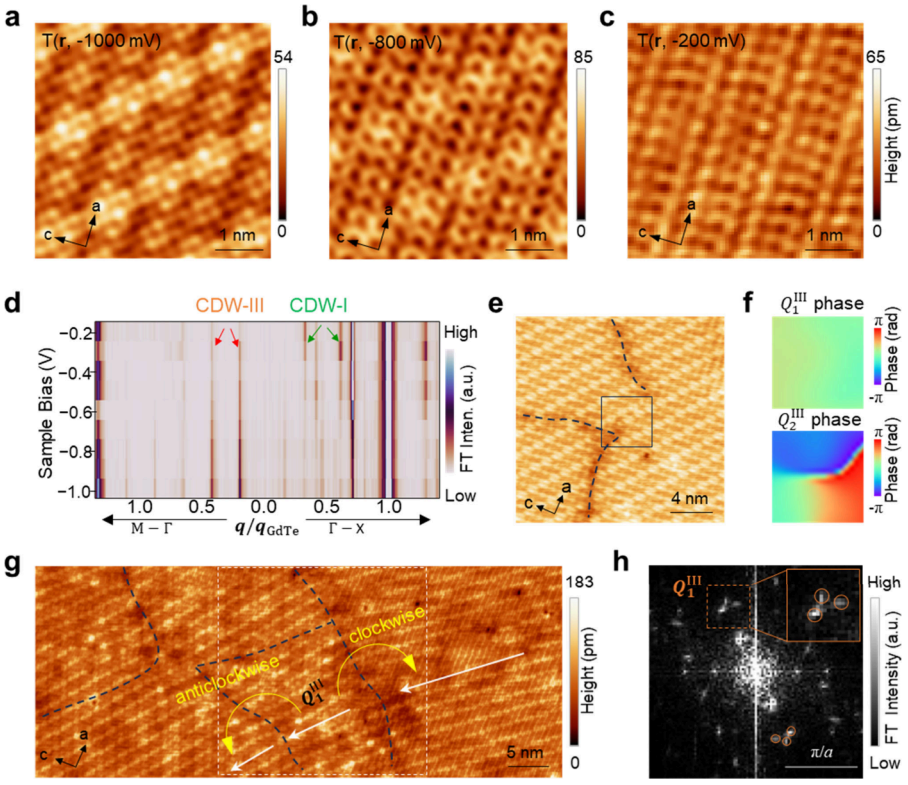

Figure 2. Energy dependence, phase shift and orientations of CDW-III orders in Domain-B. (a−c) Atomically resolved STM images acquired at different bias voltages of V_s = −1000 mV (a), −800 mV (b) and −200 mV (c), showing the gradually suppressing amplitude of CDW-III and enhancing amplitude of CDW-I with decreasing bias voltage. Tunneling parameter: I_t = 500 pA. (d) Sample bias dependence of FT cuts along the Γ−X and Γ−M directions, respectively, showing the competition between CDW-I (green arrows) and CDW-III (red arrows). (e) STM topographic images of Domain-B, showing the discontinuous phase of CDW-III (V_s = −1.0 V, I_t = 50 pA). The dashed lines mark the π-phase shift boundary. (f) Extracted phase maps of Q_1^{III} (upper panel) and Q_2^{III} (lower panel) at the region marked by a black square in (e), showing a topological defect of CDW-III. (g) STM topographic images, showing several regions with rotating CDW-III (V_s = −1 V, I_t = 50 pA). The white arrows indicate the direction of CDW-III in each region. Black dashed lines indicate the boundaries of CDW-III with distinct orientations. (h) Zoomed-in FFT of the region marked by white dashed square in (g), showing three pairs of CDW-III wavevectors (orange circles) with different orientations.

−0.4 V. Second, CDW-II is unchanged across a twin boundary of CDW-I with a 90° rotation (Figure S3). These observations demonstrate that two distinct CDW orders coexist within Domain A, rather than CDW-II being a secondary modulation derived from CDW-I.

We now turn to the charge modulations in Domain-B surface region. Topographic images reveal the coexistence of the unidirectional CDW-I and a second bidirectional CDW, hereafter referred to as CDW-III (Figure 1b). The corresponding FFT of the topographic image in Domain-B also presents a series of complex diffraction peaks (Figure 1d), where the CDW-III primitive vectors (orange circles in Figure 1d) are $\mathbf{Q}_1^{III}$ = (0.17 q, 0.17 q) and $\mathbf{Q}_2^{III}$ = (0.25 q, 0.25 q). We notice that $\mathbf{Q}_1^{III}$ and $\mathbf{Q}_2^{III}$ are both incommensurate and along diagonal (Γ−M) direction, thereby yielding a series of additional peaks (details see Figure S4). The separately filtered zoomed-in images show that CDW-III presents a bidirectional pattern in real space. Unlike the C_{2v}-symmetric CDW-II, CDW-III exhibits a C_2 symmetry that breaks the mirror symmetry parallel to ***a*** axis (Figure 1f). Atomically resolved STM images acquired at different bias voltages show that CDW-III dominates at higher bias, whereas CDW-I prevails at lower bias (Figure 2a−c and Figure S5). Consistently, further FT cuts along the Γ−X and Γ−M directions reveal a gradual suppression of CDW-I and a concurrent enhancement of CDW-III with increasing bias voltage (Figure 2d). Similar to Domain-A, we find a CDW gap of ∼400 meV in the spatially averaged dI/dV spectrum of Domain-B (Figure S6), and observe a twin boundary of CDW-I in a continuous CDW-III area, which indicates the independence of CDW-I and CDW-III (Figure S7). In addition, the CDW-III exhibits no measurable response to room temperature (up to 300 K) or perpendicular magnetic fields (up to 9 T) (Figure S8), ruling out an antiferromagnetic origin.

In contrast to the continuous phases of CDW-II, the phase of CDW-III is discontinuous. We extracted the phase maps of $\mathbf{Q}_1^{III}$ and $\mathbf{Q}_2^{III}$ in a STM image of Domain-B (Figure 2e) with two-dimensional lock-in technique,[34] respectively (see Methods and Figure S9). The phase (ϕ) map of $\mathbf{Q}_2^{III}$ exhibits π-phase frustrated boundary along the dashed black curves, whereas the phase of $\mathbf{Q}_1^{III}$ is continuous. A zoomed-in view of the frustrated region (black square) reveals a CDW topological defect (Figure 2f). In addition to a phase shift, CDW-III shows a slight real-space rotation of its propagation direction. Large-scale topographic images reveal that the propagation direction of CDW-III is not always strictly aligned with the diagonal directions, but occasionally exhibits clockwise or anticlockwise deviations of approximately 6° (Figure 2g). The FFT of a representative region marked by a white dashed square in Figure 2g shows the coexistence of CDW-III wave vectors with

https://doi.org/10.1021/acs.nanolett.6c00774
Nano Lett. 2026, 26, 5882−5890

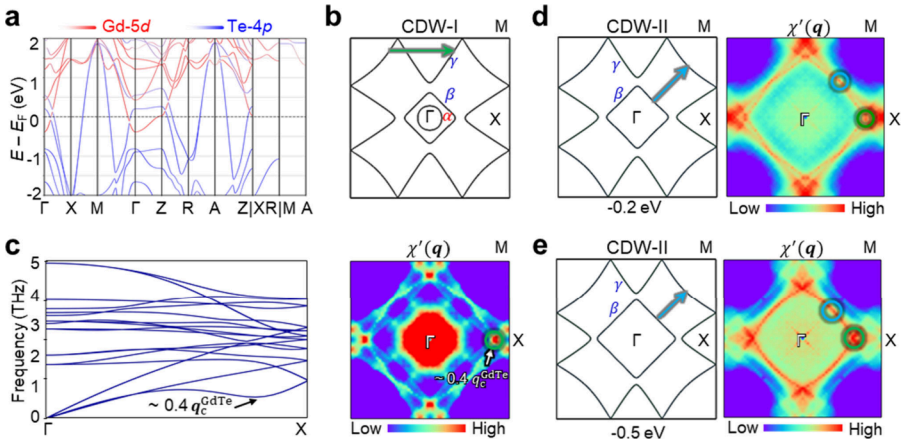

Figure 3. Formation mechanism of CDW-I and CDW-II orders in the bulk $GdTe_2$. (a) Orbital-projected band structure of the non-CDW phase $GdTe_2$ with spin−orbit coupling (SOC). (b) 2D Fermi surface with SOC at the $k_b = 0$ plane, where three Fermi pockets (α mainly from d orbitals of Gd and β,γ mainly from $p_{x,y}$ orbitals of Te layer) are shown. (c) Left: Phonon dispersion of non-CDW phase $GdTe_2$. The soft mode appears at $q = 0.4\ q_{GdTe}$. Right: Calculated Lindhard function $\chi'(q)$ corresponding to (b), suggesting the CDW wave vectors at around $0.4\ q_{GdTe}$. Note that the high $\chi'(q)$ around the Γ point comes from d orbitals of Gd, which contribute minimally to CDW formation in rare-earth tellurides. (d, e) The 2D Fermi surfaces (left) and Lindhard functions (right) at the chemical potentials of −0.2 eV (d) and −0.5 eV (e), respectively.

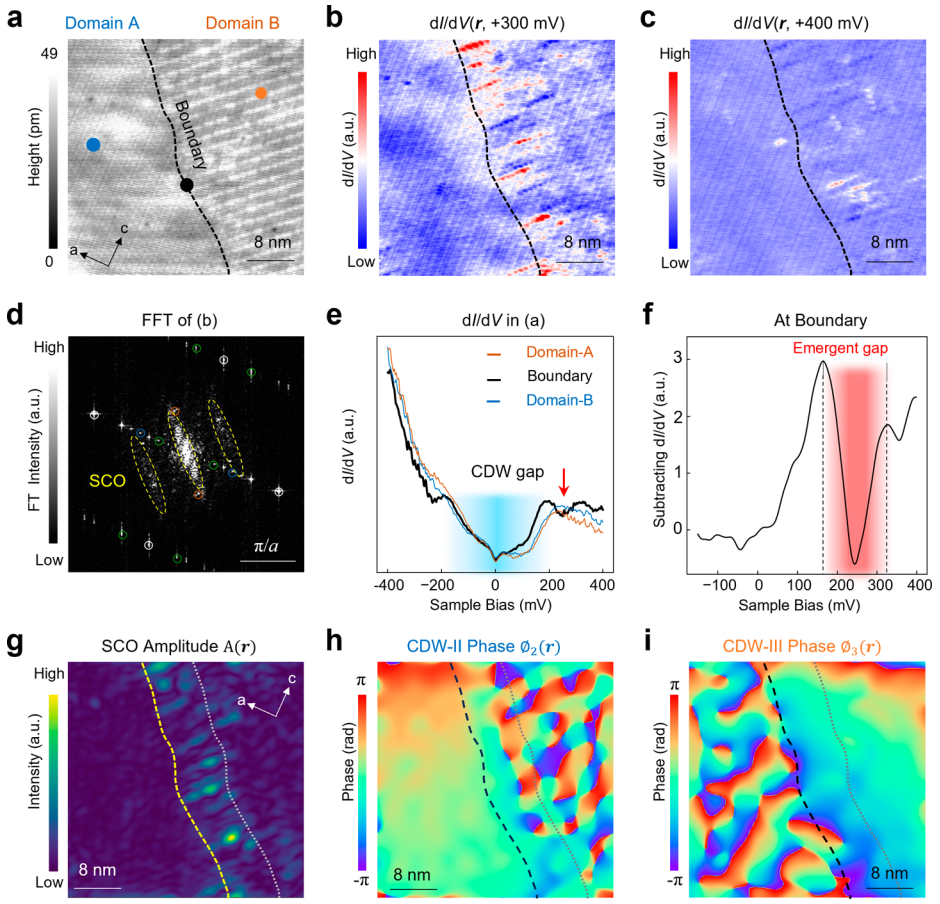

Figure 4. Emergent short-range charge orders at the domain boundary between CDW-II and CDW-III. (a) STM topographic image of an atomically sharp domain boundary (marked by the black dashed line) of CDW-II and CDW-III ($V_s = -1$ V, $I_t = 50$ pA). (b, c) dI/dV maps obtained at +300 mV (b) and +400 mV (c) showing the short-range charge order along the domain boundary. (d) FFT corresponding to (b). The yellow dashed elliptical patterns show the short-range charge orders. (e) dI/dV spectra acquired separately in Domain-A, Domain-B, and at the domain boundary. (f) The dI/dV spectrum acquired at the domain boundary by subtracting the average dI/dV spectrum measured within the domains, highlighting the gap of short-range charge orders. (g) Extracted amplitude distribution of the short-range charge orders. Dashed lines indicate the boundary of the orders. (h, i) Extracted phase maps of CDW-II (h) and CDW-III (i), showing the coherence phase of CDW-II and phase jump of CDW-III.

https://doi.org/10.1021/acs.nanolett.6c00774
Nano Lett. 2026, 26, 5882−5890

multiple orientations (Figure 2h). These rotations are accompanied by slight variations in the wave-vector magnitude, as evidenced by the real-space images and their corresponding FFTs (for details, see Figure S10a−d). To further elucidate the relationship between this rotatable CDW-III and the underlying crystal structure, we obtained atomically resolved STM images directly across a rotation boundary (Figure S10e,f). The zoomed-in image clearly demonstrates that the underlying atomic lattice remains continuous and undisturbed across the interface, while only the electronic modulation shifts its orientation, confirming that CDW-III is partially decoupled from the lattice. Remarkably, the rotation directions can be switched by applying a localized electric field with the STM tip (Figure S11), indicative of a surface-sensitive nature of CDW-III. Overall, these observations rule out a bulk-contributed lattice reconstruction as the origin of CDW-III. Notably, such a CDW state has not been observed in MBE-grown $GdTe_2$ thin films,[33] indicating that CDW-III is likely a direct consequence of the cleavage effects unique to bulk single crystals.

Given the spatial separation of multiple CDWs with distinct characterizations, it is natural to know the formation mechanism of these CDWs. Thus, we investigate the origins of multiple competing CDWs by performing DFT calculations. As shown in Figure 3a, the electronic states of bulk $GdTe_2$ are dominated by d orbitals of Gd and $p_{x,y}$ orbitals of Te layer near the Fermi level (E_F), which contribute three distinct pockets (α, β, γ) on the Fermi surface (Figure 3b). The calculated Lindhard function reveals the first CDW with a wave vector of ∼0.4 $\mathbf{q}_{GdTe}$ at E_F (right in Figure 3c), whose origin is illustrated by an arrow within the γ pocket (Figure 3b). Phonon calculations further show a soft mode at ∼0.4 $\mathbf{q}_{GdTe}$ (left in Figure 3c), consistent with the Lindhard function and suggesting that this first CDW stems from electron−phonon coupling.[35] Upon tuning the chemical potentials, the second CDW emerges with a wave vector from 0.236 to 0.354 $\mathbf{q}_{Te}$ ($\mathbf{q}_{Te}$ = (q, q)). This is supported by the DFT-calculated Fermi surfaces and Lindhard functions at E_F − 0.2 eV and E_F − 0.5 eV, where an arrow between the β and γ pockets reveals the origin of this second CDW (Figure 3d,e). We attribute these two CDWs to be the experimentally observed CDW-I and CDW-II, respectively, for the following reasons: (i) The first CDW is unidirectional and persists over a wide chemical potential range (−1 to 0 eV) with a wave vector from 0.3 to 0.4 $\mathbf{q}_{GdTe}$, consistent with the observations of CDW-I; (ii) The second CDW is bidirectional with a wave vector approaching 0.354 $\mathbf{q}_{Te}$, and exhibits stronger intensity away from E_F, matching the main features of CDW-II. Additionally, these two CDWs have also been discovered in other rare-earth ditellurides,[36,37] supporting the notion that CDW-I and CDW-II should originate from the intrinsic bulk properties of $GdTe_2$. Instead, CDW-III probably originates from a surface-induced Fermi surface reconstruction caused by surface potential at the non-vdW cleaved terminations of $GdTe_2$[38−40], making it a surface-specific CDW rather than a bulk order (details see Supplementary Note 1).

Finally, we focus on the intriguing electronic reconstruction occurring at the boundary between competing CDW orders. As discussed above, CDW-I persists as a robust background modulation over a wide energy range and remains continuous across the entire field of view. In contrast, the system hosts two distinct charge-ordered states, which occupy spatially separated regions (Domain-A and Domain-B) and give rise to a well-defined domain boundary, marked by the black dashed line in Figure 4a. Strikingly, the dI/dV maps acquired at +300 mV and +400 mV reveal pronounced stripe-like, discrete SCO confined along the boundary (Figure 4b,c). In the FT of the dI/dV map across the boundary, these SCO signals manifest as three elliptical features elongated along the Γ−X direction, as highlighted by the yellow dashed contours in Figure 4d, indicating a quasi-one-dimensional and short-range nature. A systematic bias-dependent measurement further shows that the SCO emerges predominantly within an energy window from +200 meV to +500 meV (Figure S12). The same phenomenon can also be observed at another boundary, indicating that this is not an accidental occurrence (Figure S13). By contrast, at higher energies such as − 900 meV, where SCO signatures are absent, the dI/dV maps only display a weak intensity difference between Domain-A and Domain-B without any boundary-localized features (Figure S12e). The corresponding FFT at this energy emphasizes the coexistence of three CDW wave vectors (Figure S12f). Notably, the wave vector $\mathbf{Q}_1^{II}$ of CDW-II lies very close to $\mathbf{Q}_3^{III}$ of CDW-III, making them difficult to distinguish experimentally and suggesting that CDW-III may evolve from surface-induced symmetry-breaking effects.

Importantly, tunneling spectra taken within Domain-A and Domain-B exhibit nearly identical electronic structures, indicating that the bulk electronic states of the two domains are comparable (Figure 4e). In contrast, the spectrum measured directly at the DW shows the opening of an emergent energy gap. By subtracting the averaged non-boundary spectrum, we identify an energy gap of approximately 160 meV, centered at +240 meV (Figure 4f), with gap edges located at +180 meV and +320 meV. Given that this energy scale coincides precisely with the bias range where SCO is observed, the gap is naturally attributed to the emergence of the boundary-confined charge order.

To elucidate the microscopic origin of SCO, we extract the spatial amplitude distributions of SCO, CDW-II, and CDW-III (Figure 4g and Figure S14), respectively. Across the domain boundary, the transition from Domain-A (CDW-II and CDW-I) to Domain-B (CDW-III and CDW-I) is atomically abrupt, with no gradual amplitude decay or spatial overlap between CDW-II and CDW-III. Meanwhile, SCO is predominantly localized on the Domain-B side, confined to a narrow region adjacent to the boundary (marked by dashed lines). This spatial separation unambiguously rules out a trivial superposition or interference effect of two long-range CDWs as the origin of SCO. Furthermore, atomically resolved STM topographic image confirms that the underlying lattice is perfectly continuous across the boundary without structural distortions (Figure S15), excluding the possibilities of atomic structural modulations. Combining the abrupt spatial transition of the CDW amplitudes (Figure S14), the uninterrupted atomic lattice (Figure S15), and the localized emergent gap at the interface (Figure 4f), we conclusively attribute the SCO to a genuinely emergent electronic charge order. Instead, the atomically sharp boundary frustrates the free-energy minimization of competing orders: CDW-II favors a three-dimensional, bulk-stabilized long-range order, whereas CDW-III prefers a surface-reconstructed modulation. As a result, neither order can remain energetically optimal at the boundary, naturally driving an interfacial electronic reconstruction manifested as the emergent SCO. However, similar SCO can not be observed at the twin boundary of bulk CDW-I.

In a low-energy description, the CDW order parameter $\Delta(x) = |\Delta|e^{i\phi(x)}$, where $|\Delta|$ is the amplitude, ϕ is the phase, acts as an

https://doi.org/10.1021/acs.nanolett.6c00774
Nano Lett. 2026, 26, 5882−5890

effective mass term in the Hamiltonian. The interfacial reconstruction is directly reflected in the phase ϕ evolution of the two CDW order parameters extracted by 2D lock-in technique (see Methods). The extracted phase map shows that CDW-II maintains a uniform and coherent phase throughout Domain-A (Figure 4h), whereas the phase of CDW-III undergoes a rapid spatial evolution from π to $-\pi$ near the boundary region, spatially coincident with the SCO (Figure 4i). This stark contrast reflects their profoundly different phase stiffness. The bulk-driven CDW-II acts as a rigid phase boundary condition, forcing the comparatively softer, surface-derived CDW-III to completely incorporate the interfacial phase deformation.[41] The observed abrupt phase twist therefore produces a localized *"mass kink"*, a situation well-known to generate domain-boundary bound states when the order parameter changes sign or phase abruptly.[42,43] In the present case, the mismatch in wavevector, symmetry (C_{2v} versus C_2), and phase relationship renders the CDW-II and CDW-III order parameters incompatible at the domain boundary. The resulting large CDW phase gradient $\nabla\phi$ produces an effective localized potential well that traps electronic states within a narrow energy window, giving rise to the reconstructed energy gap observed in the tunneling spectra (Figure 4e). The CDW domain boundary thus behaves as a quasi-one-dimensional electronic channel hosting emergent bound states stabilized by the competition between the two charge orders.[44] This scenario closely resembles previously reported DW-induced states, such as pair density waves at superconducting domain boundaries[45] and localized quasiparticle states generated by disrupted spin density waves.[46] The SCO observed here is therefore not a trivial modulation, but a direct manifestation of phase incompatibility between competing CDW orders and the resulting DW bound states. Such an interfacial electronic reconstruction, driven by the incompatibility of bulk and surface CDW order parameters, extends the knowledge of emergent phenomena in systems with multiple CDWs.

In summary, we directly visualize multiple competing CDWs at the surface of $GdTe_2$, including intrinsic bulk orders and a surface-specific CDW induced by symmetry breaking at the non-vdW termination. At the boundaries between these competing phases, we uncover domain-wall-confined charge order accompanied by an emergent energy gap, indicating localized electronic states arising from the incompatibility of competing order parameters. These findings redefine CDW domain walls from passive structural defects into electronically reconstructed interfaces that host confined and gapped boundary states. More broadly, our results suggest that engineered CDW domain boundaries can serve as confined one-dimensional electronic channels with tunable electronic structure, offering a promising platform for nanoscale CDW-based devices and domain-wall–defined functional architectures in low-dimensional quantum materials.

CRYSTAL GROWTH

The $GdTe_2$ single crystal was synthesized via the chemical vapor transport (CVT) method. Stoichiometric amounts of Gd and Te in a molar ratio of 1:2 were sealed in a quartz tube along with iodine (I_2) as the transport agent. The sealed tube was placed in a two-zone tubular furnace, heated to 980 °C (source zone) and 940 °C (growth zone) over 12 h, maintained at these temperatures for 7 days, and finally allowed to cool naturally to room temperature. The $GdTe_2$ single crystals were obtained in the growth zone.

STM AND STS MEASUREMENTS

For STM and STS measurements, we cleaved the samples at room temperature (~300 K) and immediately transferred them to the STM chamber, where they were cooled to 4.2 K. Experiments were performed in an ultrahigh vacuum (1×10^{-10} mbar) ultralow temperature STM system equipped with external magnetic field perpendicular to the sample surface. The lowest base temperature is 0.4 K with an electronic temperature of 650 mK (calibrated using a standard Nb superconductor). All the scanning parameters (set point voltage V_s and tunneling current I_t) of the STM topographic images are listed in the figure captions. The dI/dV spectra were acquired by a standard lock-in amplifier at a modulation frequency of 973.1 Hz, the modulation bias (V_{mod}) is listed in the figure captions. Nonmagnetic tungsten tips were fabricated via electrochemical etching and subsequently calibrated on a clean Au(111) surface, prepared by repeated cycles of sputtering with argon ions and annealing at 500 °C.

TWO-DIMENSIONAL LOCK-IN TECHNIQUE

We employed a two-dimensional lock-in technique to determine the amplitude and phase of CDW orders. For any arbitrary real space image:

$$A(\mathbf{r}) = \sum_{\mathbf{Q}} a_{\mathbf{Q}}(\mathbf{r}) e^{-i\mathbf{Q}\cdot\mathbf{r}}$$

where $a_{\mathbf{Q}}(\mathbf{r})$ is the complex amplitude at wavevector $\mathbf{Q}$ and position r. If $\mathbf{Q}$ is the wavevector of interest, it can be extracted from the Fourier transform $A(\mathbf{q})$ by shifting it back to the center and multiplying a Gaussian window with a cutoff length σ in q-space. The approximate complex amplitude in real space $A_{\mathbf{Q}}(\mathbf{r})$ can be obtained by inverse Fourier transform as following:

$$A_{\mathbf{Q}}(\mathbf{r}) = F^{-1}[A_{\mathbf{Q}}(\mathbf{q})] = \int d\mathbf{R} A(\mathbf{R}) e^{i\mathbf{Q}\cdot\mathbf{R}} e^{-(r-\mathbf{R})^2/2\sigma^2}$$

Thus, using this technique, the amplitude $|A_{\mathbf{Q}}(\mathbf{r})|$ and spatial phase $\Phi^A_{\mathbf{Q}}(\mathbf{r})$ of the modulation at $\mathbf{Q}$ can be written as

$$|A_{\mathbf{Q}}(\mathbf{r})| = \sqrt{\mathrm{Re}A_{\mathbf{Q}}(\mathbf{r})^2 + \mathrm{Im}\,A_{\mathbf{Q}}(\mathbf{r})^2}$$

$$\Phi^A_{\mathbf{Q}}(\mathbf{r}) = \tan^{-1}\frac{\mathrm{Im}\,A_{\mathbf{Q}}(\mathbf{r})}{\mathrm{Re}\,A_{\mathbf{Q}}(\mathbf{r})}$$

For Figure 2f, the Gaussian filter order is 12 and the filter length scale is 0.176 q in momentum space, corresponding to 2.5 nm in real space. For Figure 4h, I, the Gaussian filter order is 16 and the filter length scale is 0.198 q in momentum space, corresponding to 2.2 nm in real space.

DFT CALCULATIONS

DFT calculations were performed via Vienna *Ab-initio* Simulation Package (VASP)[47] using the Perdew–Burke–Ernzerhof (PBE) exchange-correlation functional.[48] We employed a plane-wave cutoff of 500 eV and set convergence thresholds to 0.01 eV/Å for atomic relaxations and 10^{-6} eV for electronic self-consistency. We excluded the 4*f* electrons of Gd from the pseudopotential, as they are highly localized and lie far away from the Fermi level. SOC was included in all

https://doi.org/10.1021/acs.nanolett.6c00774
Nano Lett. 2026, 26, 5882–5890

electronic structure calculations, and a 60 × 60 *k*-mesh was used for the 2D Fermi surface and Lindhard function. This function represents the real part of bare electronic susceptibility and is defined as follows:[35]

$$\chi'(\mathbf{q}, T) = -\frac{2}{N_{\mathbf{k}}} \sum_{\mathbf{k},mn} \frac{f(\varepsilon_{n,\mathbf{k}+\mathbf{q}}) - f(\varepsilon_{m,\mathbf{k}})}{\varepsilon_{n,\mathbf{k}+\mathbf{q}} - \varepsilon_{m,\mathbf{k}}}$$

where $\varepsilon_{n,\mathbf{k}}$ are Kohn−Sham eigenvalues of the *n*th band at momentum $\mathbf{k}$ and *f* is the Fermi−Dirac distribution. We fixed the temperature (T) to 100 K. Note that the prominent peak in $\chi'(\mathbf{q}, T)$ typically indicates a CDW wave vector driven by electron−phonon coupling.[35] The phonon dispersions of non-CDW phase $GdTe_2$ were calculated by density functional perturbation theory, within a 4 × 4 × 2 supercell.

■ ASSOCIATED CONTENT

Supporting Information

The Supporting Information is available free of charge at https://pubs.acs.org/doi/10.1021/acs.nanolett.6c00774.

Discussion on the possible formation mechanism of surface-induced CDW-III, spatially averaged d*I*/d*V* spectra of CDW gaps, additional data of the bias-dependence of CDW-II and CDW-III, STM observations of CDW-I twin boundaries and orthogonal rotations, stability of CDW-III under varying temperatures and magnetic fields, extracted phase and amplitude maps, manipulation of the CDW-III rotation by STM tip electric fields, and additional data and analysis of emergent short-range charge orders and continuous atomic lattices across domain boundaries (PDF)

■ AUTHOR INFORMATION

Corresponding Author

Hui Chen − *Beijing National Center for Condensed Matter Physics and Institute of Physics, Chinese Academy of Sciences, Beijing 100190, PR China; School of Physical Sciences, University of Chinese Academy of Sciences, Beijing 100190, PR China; Hefei National Laboratory, Hefei, Anhui 230088, PR China;* orcid.org/0000-0002-3369-8113; Email: hchenn04@iphy.ac.cn

Authors

Zhongyi Cao − *Beijing National Center for Condensed Matter Physics and Institute of Physics, Chinese Academy of Sciences, Beijing 100190, PR China; School of Physical Sciences, University of Chinese Academy of Sciences, Beijing 100190, PR China*

Wen-Han Dong − *State Key Laboratory of Low-Dimensional Quantum Physics and Department of Physics, Tsinghua University, Beijing 100084, China;* orcid.org/0000-0001-8356-276X

Yanhao Shi − *Beijing National Center for Condensed Matter Physics and Institute of Physics, Chinese Academy of Sciences, Beijing 100190, PR China; School of Physical Sciences, University of Chinese Academy of Sciences, Beijing 100190, PR China*

Qi Qi − *Beijing National Center for Condensed Matter Physics and Institute of Physics, Chinese Academy of Sciences, Beijing 100190, PR China; School of Physical Sciences, University of Chinese Academy of Sciences, Beijing 100190, PR China*

Haitao Yang − *Beijing National Center for Condensed Matter Physics and Institute of Physics, Chinese Academy of Sciences, Beijing 100190, PR China; School of Physical Sciences, University of Chinese Academy of Sciences, Beijing 100190, PR China; Hefei National Laboratory, Hefei, Anhui 230088, PR China;* orcid.org/0000-0003-4304-9835

Hong-Jun Gao − *Beijing National Center for Condensed Matter Physics and Institute of Physics, Chinese Academy of Sciences, Beijing 100190, PR China; School of Physical Sciences, University of Chinese Academy of Sciences, Beijing 100190, PR China; Hefei National Laboratory, Hefei, Anhui 230088, PR China;* orcid.org/0000-0002-6766-0623

Complete contact information is available at: https://pubs.acs.org/10.1021/acs.nanolett.6c00774

Author Contributions

⊥Z. C., H. C., W.-H. D. and Y. S. contributed equally to this work. H. C. designed the experiments. Z. C., H. C. and Y. S. performed the STM/STS experiments and data analysis. Q. Q. and H. Y. prepared the $GdTe_2$ samples. W.-H. D. performed the DFT calculations. Z. C., H. C., W.-H. D. and H.-J. G. wrote the manuscript with input from all other authors.

Notes

The authors declare no competing financial interest.

■ ACKNOWLEDGMENTS

This work is supported by the National Key Research and Development Project of China (Grant No. 2022YFA1204100), the National Natural Science Foundation of China (Grants No. 62488201, 92580202 and 12504078), and the CAS Project for Young Scientists in Basic Research (Grant No. YSBR-003).

■ REFERENCES

(1) Catalan, G.; Seidel, J.; Ramesh, R.; Scott, J. F. Domain wall nanoelectronics. *Rev. Mod. Phys.* **2012**, *84* (1), 119−156.

(2) Barja, S.; Wickenburg, S.; Liu, Z.-F.; Zhang, Y.; Ryu, H.; Ugeda, M. M.; Hussain, Z.; Shen, Z.-X.; Mo, S.-K.; Wong, E.; Salmeron, Miquel B.; Wang, F.; Crommie, M. F.; Ogletree, D. F.; Neaton, Jeffrey B.; Weber-Bargioni, A. Charge density wave order in 1D mirror twin boundaries of single-layer $MoSe_2$. *Nat. Phys.* **2016**, *12* (8), 751−756.

(3) Huang, F.-T.; Cheong, S.-W. Aperiodic topological order in the domain configurations of functional materials. *Nat. Rev. Mater.* **2017**, *2* (3), 17004.

(4) Jiang, L.; Wang, S.; Shi, Z.; Jin, C.; Utama, M. I. B.; Zhao, S.; Shen, Y.-R.; Gao, H.-J.; Zhang, G.; Wang, F. Manipulation of domain-wall solitons in bi- and trilayer graphene. *Nat. Nanotechnol.* **2018**, *13* (3), 204−208.

(5) Lin, C.-C.; Hu, Y.; Kim, J.; Lou, D.; Bhat, A.; Kavle, P.; Kim, T. Y.; Dames, C.; Liu, S.; Martin, L. W. Domain-Wall Enhanced Pyroelectricity. *Phys. Rev. X* **2025**, *15* (1), 011063.

(6) Yao, Q.; Park, J. W.; Oh, E.; Yeom, H. W. Engineering Domain Wall Electronic States in Strongly Correlated van der Waals Material of 1T-TaS_2. *Nano Lett.* **2021**, *21* (22), 9699−9705.

(7) Peierls, R. E. S.; Roberts, L. D. Quantum theory of solids. *Phys. Today* **1956**, *9*, 29.

(8) Baggioli, M.; Goutéraux, B. Colloquium: Hydrodynamics and holography of charge density wave phases. *Rev. Mod. Phys.* **2023**, *95* (1), 011001.

(9) Hu, Y.; Zhang, T.; Zhao, D.; Chen, C.; Ding, S.; Yang, W.; Wang, X.; Li, C.; Wang, H.; Feng, D.; Zhang, T. Real-space observation of incommensurate spin density wave and coexisting charge density wave on Cr (001) surface. *Nat. Commun.* **2022**, *13* (1), 445.

(10) Han, X.; Chen, H.; Cao, Z.; Guo, J.; Tuo, C.; Li, M.-R.; Fei, F.; Tan, H.; Guo, J.; Shi, Y.; Zhou, R.; Wang, R.; Zhao, Z.; Yang, H.; Song, F.; Yao, H.; Yan, B.; Zhu, S.; Wang, Z.; Gao, H.-J. Unconventional spin-intertwined charge density wave in magnetic phases of kagome metal $GdTi_3Bi_4$. *Nat. Commun.* **2026**, *17* (1), 2667.
(11) Chang, J.; Blackburn, E.; Holmes, A. T.; Christensen, N. B.; Larsen, J.; Mesot, J.; Liang, R.; Bonn, D. A.; Hardy, W. N.; Watenphul, A.; Zimmermann, M. v.; Forgan, E. M.; Hayden, S. M. Direct observation of competition between superconductivity and charge density wave order in $YBa_2Cu_3O_{6.67}$. *Nat. Phys.* **2012**, *8* (12), 871−876.
(12) Lian, C.-S.; Si, C.; Duan, W. Unveiling Charge-Density Wave, Superconductivity, and Their Competitive Nature in Two-Dimensional $NbSe_2$. *Nano Lett.* **2018**, *18* (5), 2924−2929.
(13) Agterberg, D. F.; Davis, J. C. S.; Edkins, S. D.; Fradkin, E.; Van Harlingen, D. J.; Kivelson, S. A.; Lee, P. A.; Radzihovsky, L.; Tranquada, J. M.; Wang, Y. The Physics of Pair-Density Waves: Cuprate Superconductors and Beyond. *Annual Review of Condensed Matter Physics* **2020**, *11*, 231−270.
(14) Chen, H.; Yang, H.; Hu, B.; Zhao, Z.; Yuan, J.; Xing, Y.; Qian, G.; Huang, Z.; Li, G.; Ye, Y.; Ma, S.; Ni, S.; Zhang, H.; Yin, Q.; Gong, C.; Tu, Z.; Lei, H.; Tan, H.; Zhou, S.; Shen, C.; Dong, X.; Yan, B.; Wang, Z.; Gao, H.-J. Roton pair density wave in a strong-coupling kagome superconductor. *Nature* **2021**, *599* (7884), 222−228.
(15) Brazovskii, S.; Nattermann, T. Pinning and sliding of driven elastic systems: from domain walls to charge density waves. *Adv. Phys.* **2004**, *53* (2), 177−252.
(16) Schuricht, D.; Essler, F. H. L.; Jaefari, A.; Fradkin, E. Local Density of States of One-Dimensional Mott Insulators and Charge-Density Wave States with a Boundary. *Phys. Rev. Lett.* **2008**, *101* (8), 086403.
(17) Zong, A.; Shen, X.; Kogar, A.; Ye, L.; Marks, C.; Chowdhury, D.; Rohwer, T.; Freelon, B.; Weathersby, S.; Li, R.; Yang, J.; Checkelsky, J.; Wang, X.; Gedik, N. Ultrafast manipulation of mirror domain walls in a charge density wave. *Sci. Adv.* **2018**, *4* (10), No. eaau5501.
(18) Lee, S.; Collini, J.; Sun, S. X. L.; Mitrano, M.; Guo, X.; Eckberg, C.; Paglione, J.; Fradkin, E.; Abbamonte, P. Multiple Charge Density Waves and Superconductivity Nucleation at Antiphase Domain Walls in the Nematic Pnictide $Ba_{1-x}Sr_xNi_2As_2$. *Phys. Rev. Lett.* **2021**, *127* (2), 027602.
(19) Sajan, S.; Guo, H.; Agarwal, T.; Sánchez-Ramírez, I.; Patra, C.; Vergniory, M. G.; de Juan, F.; Singh, R. P.; Ugeda, M. M. Atomic-Scale Mapping of Superconductivity in the Incoherent CDW Mosaic Phase of a Transition Metal Dichalcogenide. *Nano Lett.* **2025**, *25* (16), 6654−6660.
(20) Park, J. W.; Lee, J.; Yeom, H. W. Zoology of domain walls in quasi-2D correlated charge density wave of 1T-TaS_2. *npj Quantum Mater.* **2021**, *6* (1), 32.
(21) Joe, Y. I.; Chen, X. M.; Ghaemi, P.; Finkelstein, K. D.; de la Peña, G. A.; Gan, Y.; Lee, J. C. T.; Yuan, S.; Geck, J.; MacDougall, G. J.; Chiang, T. C.; Cooper, S. L.; Fradkin, E.; Abbamonte, P. Emergence of charge density wave domain walls above the superconducting dome in 1T-$TiSe_2$. *Nat. Phys.* **2014**, *10* (6), 421−425.
(22) Cho, D.; Gye, G.; Lee, J.; Lee, S.-H.; Wang, L.; Cheong, S.-W.; Yeom, H. W. Correlated electronic states at domain walls of a Mott-charge-density-wave insulator 1T-TaS_2. *Nat. Commun.* **2017**, *8* (1), 392.
(23) Lee, J.; Park, J. W.; Cho, G. Y.; Yeom, H. W. Mobile Kink Solitons in a Van der Waals Charge-Density-Wave Layer. *Adv. Mater.* **2023**, *35* (29), 2300160.
(24) Zhang, H.; Chen, H.; Huang, Z.; Wang, Z.-A.; Lv, S.; Xian, G.; Guo, H.; Yang, H.; Gao, H.-J. Tuning Bound States of Symmetry-Breaking Vortices via Unidirectional Charge Density Wave in a Transition-Metal Dichalcogenide Superconductor. *Nano Lett.* **2025**, *25* (47), 16650−16657.
(25) Song, X.; Liu, L.; Yang, H.; Chen, Y.; Huang, X.; Huang, Z.; Yang, H.; Zhang, T.; Huang, Y.; Gao, H. J.; Wang, Y. Unusual Geometric and Electronic Structures at Domain Boundaries in a Heterochiral Charge Density Wave Superlattice. *ACS Nano* **2024**, *18* (49), 33398−33404.
(26) Kim, H.; Jin, K. H.; Yeom, H. W. Electronically Seamless Domain Wall of Chiral Charge Density Wave in 1T-$TiSe_2$. *Nano Lett.* **2024**, *24* (45), 14323−14328.
(27) Yumigeta, K.; Qin, Y.; Li, H.; Blei, M.; Attarde, Y.; Kopas, C.; Tongay, S. Advances in Rare-Earth Tritelluride Quantum Materials: Structure, Properties, and Synthesis. *Adv. Sci.* **2021**, *8* (12), 2004762.
(28) Malliakas, C. D.; Iavarone, M.; Fedor, J.; Kanatzidis, M. G. Coexistence and Coupling of Two Distinct Charge Density Waves in Sm_2Te_5. *J. Am. Chem. Soc.* **2008**, *130* (11), 3310−3312.
(29) Hu, B. F.; Cheng, B.; Yuan, R. H.; Dong, T.; Wang, N. L. Coexistence and competition of multiple charge-density-wave orders in rare-earth tritellurides. *Phys. Rev. B* **2014**, *90* (8), 085105.
(30) Xiao, K.; Dong, W.-H.; Wang, X.; Yu, J.; Fu, D.; Hu, Z.; Guo, Y.; Zhang, Q.; Hou, X.; Guo, Y.; Yang, L.; Xu, Y.; Tang, P.; Duan, W.; Xue, Q.; Li, W. Hidden Charge Order and Multiple Electronic Instabilities in $EuTe_4$. *Nano Lett.* **2024**, *24* (25), 7681−7687.
(31) Cao, Z.-Y.; Chen, H.; Qian, G.-J.; Shi, Y.-H.; Qi, Q.; Han, X.-H.; Yang, H.-T.; Gao, H.-J. Tuning the charge density wave and low-energy magnetic states with nanoscale strains in $GdTe_3$. *Chin. Phys. Lett.* **2025**, *42* (10), 100702.
(32) Tomic, A.; Rak, Z.; Veazey, J. P.; Malliakas, C. D.; Mahanti, S. D.; Kanatzidis, M. G.; Tessmer, S. H. Scanning tunneling microscopy study of the $CeTe_3$ charge density wave. *Phys. Rev. B* **2009**, *79* (8), 085422.
(33) Cai, X.; Xu, Z.; An, R.; Wu, J.; Ji, S.-H.; Li, N.; Chen, X. Charge Density Waves in $GdTe_2$ Thin Films. *J. Phys. Chem. C* **2023**, *127* (22), 10730−10736.
(34) Lawler, M. J.; Fujita, K.; Lee, J.; Schmidt, A. R.; Kohsaka, Y.; Kim, C. K.; Eisaki, H.; Uchida, S.; Davis, J. C.; Sethna, J. P.; Kim, E.-A. Intra-unit-cell electronic nematicity of the high-Tc copper-oxide pseudogap states. *Nature* **2010**, *466* (7304), 347−351.
(35) Johannes, M. D.; Mazin, I. I. Fermi surface nesting and the origin of charge density waves in metals. *Phys. Rev. B* **2008**, *77* (16), 165135.
(36) Shim, J. H.; Kang, J. S.; Min, B. I. Electronic Structures of RTe_2 (R = La, Ce): A Clue to the Pressure-Induced Superconductivity in $CeTe_{1.82}$. *Phys. Rev. Lett.* **2004**, *93* (15), 156406.
(37) Kang, J. S.; Kim, D. H.; Lee, H. J.; Hwang, J.; Lee, H.-K.; Kim, H. D.; Min, B. H.; Lee, K. E.; Kwon, Y. S.; Kim, J. W.; Kim, K.; Kim, B. H.; Min, B. I. Fermi surface reconstruction in $CeTe_2$ induced by charge density waves investigated via angle resolved photoemission. *Phys. Rev. B* **2012**, *85* (8), 085104.
(38) Reticcioli, M.; Wang, Z.; Schmid, M.; Wrana, D.; Boatner, L. A.; Diebold, U.; Setvin, M.; Franchini, C. Competing electronic states emerging on polar surfaces. *Nat. Commun.* **2022**, *13* (1), 4311.
(39) Reticcioli, M.; Setvin, M.; Hao, X.; Flauger, P.; Kresse, G.; Schmid, M.; Diebold, U.; Franchini, C. Polaron-Driven Surface Reconstructions. *Phys. Rev. X* **2017**, *7* (3), 031053.
(40) Enterkin, J. A.; Subramanian, A. K.; Russell, B. C.; Castell, M. R.; Poeppelmeier, K. R.; Marks, L. D. A homologous series of structures on the surface of $SrTiO_3$(110). *Nat. Mater.* **2010**, *9* (3), 245−248.
(41) Liu, L.; Zhu, C.; Liu, Z. Y.; Deng, H.; Zhou, X. B.; Li, Y.; Sun, Y.; Huang, X.; Li, S.; Du, X.; Wang, Z.; Guan, T.; Mao, H.; Sui, Y.; Wu, R.; Yin, J.-X.; Cheng, J. G.; Pan, S. H. Thermal Dynamics of Charge Density Wave Pinning in $ZrTe_3$. *Phys. Rev. Lett.* **2021**, *126* (25), 256401.
(42) Jackiw, R.; Rebbi, C. Solitons with fermion number 1/2. *Physical Review D* **1976**, *13* (12), 3398−3409.
(43) Sehayek, D.; Thakurathi, M.; Burkov, A. A. Charge density waves in Weyl semimetals. *Phys. Rev. B* **2020**, *102* (11), 115159.
(44) Yan, S.; Iaia, D.; Morosan, E.; Fradkin, E.; Abbamonte, P.; Madhavan, V. Influence of Domain Walls in the Incommensurate Charge Density Wave State of Cu Intercalated 1T-$TiSe_2$. *Phys. Rev. Lett.* **2017**, *118* (10), 106405.

https://doi.org/10.1021/acs.nanolett.6c00774
Nano Lett. 2026, 26, 5882−5890

(45) Liu, Y.; Wei, T.; He, G.; Zhang, Y.; Wang, Z.; Wang, J. Pair density wave state in a monolayer high-T_c iron-based superconductor. *Nature* **2023**, *618* (7967), 934−939.
(46) Hu, Y.; Wang, X.; Chen, C.; Zhang, Q.; Zhao, D.; Zhang, T.; Wang, C.; Wang, Q.-H.; Feng, D.; Zhang, T. Discovery of Itinerant Magnetic Domain Wall and Quasiparticle Boundary State in Spin-Density-Waves. *arXiv* **2024**, DOI: 10.48550/arXiv.2402.15999, (accessed 2026-04-03).
(47) Kresse, G.; Furthmüller, J. Efficient iterative schemes for ab initio total-energy calculations using a plane-wave basis set. *Phys. Rev. B* **1996**, *54* (16), 11169−11186.
(48) Perdew, J. P.; Burke, K.; Ernzerhof, M. Generalized Gradient Approximation Made Simple. *Phys. Rev. Lett.* **1996**, *77* (18), 3865−3868.

https://doi.org/10.1021/acs.nanolett.6c00774
Nano Lett. 2026, 26, 5882−5890